

5111-183

1
2
3
4
5 **Redox state of the Neoproterozoic Earth environment**
6

7
8
9
10 Aubrey L. Zerkle^{1,2*}, Mark W. Claire^{3,4}, Shawn D. Domagal-Goldman^{3,5}, James Farquhar¹, and
11 Simon W. Poulton²

12 ¹Department of Geology and ESSIC, University of Maryland, College Park, MD, USA

13 ²School of Civil Engineering and Geosciences, Newcastle University, Drummond Building,
14 Newcastle upon Tyne, NE1 7RU, UK

15 ³Virtual Planetary Laboratory, University of Washington, Seattle, WA, USA

16 ⁴School of Environmental Sciences, University of East Anglia, Norwich, UK

17 ⁵NASA Headquarters, Washington, D.C., USA
18
19

20
21
22 Submitted to *Nature Geoscience*, 4 May, 2011

23 Resubmitted 28 October, 2011
24

25 *corresponding author: aubrey.zerkle@ncl.ac.uk
26

27

28 **A Titan-like organic haze has been hypothesized for Earth's atmosphere prior to**
29 **widespread surface oxygenation ~2.45 billion years ago (Ga). We present a high-resolution**
30 **record of quadruple sulfur isotopes, carbon isotopes, and Fe speciation from the ~2.65-2.5**
31 **Ga Ghaap Group, South Africa, which suggest a linkage between organic haze and the**
32 **biogeochemical cycling of carbon, sulfur, oxygen, and iron on the Archean Earth. These**
33 **sediments provide evidence for oxygen production in microbial mats and localized**
34 **oxygenation of surface waters. However, this oxygen production occurred under a reduced**
35 **atmosphere which existed in multiple distinct redox states that correlate to changes in**
36 **carbon and sulfur isotopes. The data are corroborated by photochemical model results**
37 **that suggest bi-stable transitions between organic haze and haze-free atmospheric**
38 **conditions in the Archean. These geochemical correlations also extend to other datasets,**
39 **indicating that variations in the character of anomalous sulfur fractionation could provide**
40 **insight into the role of carbon-bearing species in the reducing Archean atmosphere.**

41 The Campbellrand-Malmani carbonate platform of the ~2.65-2.5 billion years old (Ga)
42 Ghaap Group (Transvaal Supergroup, South Africa¹) is one of the oldest carbonate platforms on
43 Earth. Molybdenum concentrations and isotopes², Re/Mo ratios³ and N isotope systematics⁴ all
44 suggest biological production of O₂ in surface waters during deposition of the upper part of the
45 succession at ~2.5 Ga. This suggestion of significant O₂ production prior to Earth's first Great
46 Oxidation Event⁵ is supported by nutrient and trace metal systematics in coeval successions from
47 other areas⁶⁻⁹. However, production of O₂ apparently did not lead to a pervasive rise in
48 atmospheric oxygen levels⁷.

49 Here, we focus on the lower part of the Ghaap Group, spanning the top of the Boomplaas
50 Formation through the lower part of the Upper Nauga Formation (Fig. 1). Our samples come

51 from drillcore GKF01, and represent deposition primarily below wave base in a slope
52 environment, with cyclic units of microbialites passing upwards into slope carbonates¹.
53 Radiometric age constraints place the base of the core at $\sim 2.65 \pm 0.08$ Ga and the top of the
54 measured section (within the Upper Nauga) at ~ 2.5 Ga¹⁰. The succession is exceptionally well-
55 preserved, having experienced only gentle tectonic warping and sub-greenschist facies
56 metamorphism¹¹.

57 **Oxygenation of the Neoproterozoic oceans**

58 Fe speciation analyses reflect water column redox conditions at the time of deposition,
59 and show significant variations throughout the section (Fig. 1; Table S1). Many samples have
60 elevated ratios of highly reactive Fe ($Fe_{\text{carbonates}} + Fe_{\text{oxides}} + Fe_{\text{magnetite}} + Fe_{\text{pyrite}}$) to total Fe
61 ($Fe_{\text{HR}}/Fe_{\text{T}} > 0.38$), indicating deposition from an anoxic water column¹². For those samples
62 exhibiting high $Fe_{\text{HR}}/Fe_{\text{T}}$, the ratios of pyrite to highly reactive Fe ($Fe_{\text{py}}/Fe_{\text{HR}}$) generally fall
63 below 0.7-0.8, suggesting that when the bottom waters were anoxic, ferruginous (Fe(II)-rich)
64 rather than euxinic (sulfide-rich) conditions were dominant¹³. Other samples representing
65 shallow water deposition (microbialites of the Monteville Fm) or transported shallow-water
66 deposits (the Lokammona), fall close to the average oxic Phanerozoic signal¹², suggesting
67 formation from an oxic water column¹³. The low $Fe_{\text{HR}}/Fe_{\text{T}}$ ratios and correlative facies
68 assemblages imply that cyanobacterial O_2 production in microbial mats resulted in oxygenation
69 of shallow surface waters as early as ~ 2.65 Ga.

70 Cyanobacterial oxygen production is further supported by trends in $\delta^{34}\text{S}$ and $\Delta^{33}\text{S}$. Sulfur
71 isotope values for the majority of the section fall on or near a linear trend in $\delta^{34}\text{S}$ versus $\Delta^{33}\text{S}$ that
72 has been described in Archean samples ($\Delta^{33}\text{S} = 0.9 \times \delta^{34}\text{S}$)¹⁴ (Fig. 2A). This trend is interpreted
73 to reflect mixing between sulfides formed from two primary atmospheric sources carrying

74 opposite sulfur mass independent fractionation (S-MIF) signals – e.g., an oxidized source
75 (sulfate) with negative $\Delta^{33}\text{S}$ and a zero valent source (S_8) with positive $\Delta^{33}\text{S}$. Samples associated
76 with microbial mats of the upper Monteville and the Lower Nauga have positive $\Delta^{33}\text{S}$ values that
77 plot parallel to the primary Archean array, but are enriched in ^{34}S by ~ 3 to 7‰ (Fig. 2A). This
78 trend could not result from changes in sulfate reduction fractionations alone, as this scenario
79 would only rotate the array. We suggest this association reflects formation of pyrite from a
80 residual pool of sulfide generated within the microbial mats¹⁵ that was partially oxidized via O_2
81 near the mat surface, enriching the sulfide in ^{34}S (see Supplementary Information, SI, for further
82 discussion).

83 **Redox state of the Neoproterozoic atmosphere**

84 Covariations in $\Delta^{33}\text{S}$, $\Delta^{36}\text{S}$, and carbon isotope data reveal an important connection
85 between the Neoproterozoic sulfur and carbon cycles. Quadruple sulfur isotope values vary
86 considerably upcore (Fig. 1; Table S2), but all show S-MIF signals reflecting photochemical
87 production¹⁶ in an atmosphere devoid of significant O_2 ¹⁷. Samples from the Boomplaas and
88 Lokammona Formations form a linear array in $\Delta^{33}\text{S}$ versus $\Delta^{36}\text{S}$, with a slope in $\Delta^{36}\text{S}/\Delta^{33}\text{S}$ of
89 approximately -0.96 (Fig. 2B). This slope is close to the reference line defined by previous
90 measurements of Archean sulfide and sulfate minerals (~ 0.9), and is also interpreted to reflect
91 mixing of sulfur from two or more atmospheric sources¹⁶. In several distinct intervals within the
92 overlying section, the samples preserve $\Delta^{33}\text{S}$ and $\Delta^{36}\text{S}$ values that form arrays rotating in a
93 clockwise manner, forming steeper slopes in $\Delta^{36}\text{S}/\Delta^{33}\text{S}$, approaching -1.5 (Fig. 2B). The data
94 preserve a continuum of $\Delta^{36}\text{S}/\Delta^{33}\text{S}$ slopes between ~ 0.9 and -1.5, and extend to highly positive
95 $\Delta^{33}\text{S}$ regardless of $\Delta^{36}\text{S}/\Delta^{33}\text{S}$. Biological sulfur cycling can produce scatter in the $\Delta^{36}\text{S}$ intercept,
96 since sulfate reduction can affect $\Delta^{36}\text{S}$ much more than $\Delta^{33}\text{S}$ ¹⁸ (Fig. S1). However, a rotation of

97 the arrays to different $\Delta^{36}\text{S}/\Delta^{33}\text{S}$ slopes instead implies a change in the nature of the primary S-
98 MIF signature, either due to a change in $\Delta^{36}\text{S}/\Delta^{33}\text{S}$ for a single atmospheric signal, or due to
99 variable amounts of mixing between two or more atmospheric sources with different $\Delta^{36}\text{S}/\Delta^{33}\text{S}$.
100 Samples with the greatest deviation in $\Delta^{36}\text{S}/\Delta^{33}\text{S}$ occur in three distinct zones, at around 1400 m,
101 1100 m, and 800 m depth in the core. These zones correspond to intervals exhibiting highly ^{13}C -
102 depleted organic matter, falling to $\delta^{13}\text{C}_{\text{org}}$ values lower than -40‰ (Fig. 1; Fig. S2). Negative
103 excursions in $\delta^{13}\text{C}_{\text{org}}$ are typically interpreted to reflect higher CH_4 fluxes and an increased
104 contribution of methanotrophic biomass to sedimentary organic matter. A significant amount of
105 methane oxidation (methanotrophy) in the modern oceans occurs anaerobically¹⁹; however,
106 $\text{Fe}_{\text{HR}}/\text{Fe}_{\text{T}}$ ratios near Phanerozoic oxic values in some of the ^{13}C -depleted samples suggest that
107 methanotrophy could also have proceeded via O_2 (Fig. 1).

108 A closer examination of previously published Neoproterozoic sulfur isotope data reveals
109 similar correlations between changes in $\Delta^{36}\text{S}/\Delta^{33}\text{S}$ slope and $\delta^{13}\text{C}_{\text{org}}$ in ~2.5 Ga sections in
110 South Africa (the Gamohaan Formation) and in Western Australia (the Mount McRae Shale)⁷
111 (Fig. S3). Samples forming an array with $\Delta^{36}\text{S}/\Delta^{33}\text{S}$ of -1.5 have also been reported for the ~2.73
112 Ga Tumbiana Formation of the Fortescue Group of Western Australia²⁰, which preserves a large
113 global negative $\delta^{13}\text{C}_{\text{org}}$ excursion down to -60‰²¹. We suggest that the correlation between
114 negative $\delta^{13}\text{C}_{\text{org}}$ excursions and $\Delta^{36}\text{S}/\Delta^{33}\text{S}$ anomalies in two sections and over ~200 million
115 years implies a global connection between methane and variations in atmospheric S-MIF signals.

116 **Modeling the Neoproterozoic atmosphere and hypotheses for S-MIF production**

117 Interpreting the magnitude of S-MIF in the geologic record requires knowledge of the
118 production, transformation, and mass partitioning of atmospheric sulfur, as well as subsequent
119 biogeochemical pathways to sedimentation. Recently measured²² absorption spectra for $^{32}\text{SO}_2$,

120 $^{33}\text{SO}_2$ and $^{34}\text{SO}_2$ help constrain S-MIF production by SO_2 photolysis and imply that changing
121 concentrations of UV absorbers²³ (such as organic haze^{20,24} formed at high atmospheric
122 $\text{CH}_4:\text{CO}_2$) might influence the S-MIF signature. S-MIF from SO_2 photolysis could also be
123 supplemented by other mass-independent kinetic isotope effects²⁵⁻²⁷, in reactions such as SO
124 photolysis, $\text{S}+\text{S}_2 \rightarrow \text{S}_3$, CS_2 photolysis^{28,29}, or the production/destruction of excited-state SO_2 .
125 Generation of significant S-MIF via any reaction other than SO_2 photolysis remains hypothetical
126 but worthy of future research given that multiple source reactions might help explain the data²⁵.
127 S-MIF, once created, partitions into all atmospheric sulfur species, and requires the simultaneous
128 presence of two (or more) atmospheric exit channels for preservation¹⁷. Furthermore, these exit
129 channels vary as a function of atmospheric methane, oxygen, and sulfur concentrations^{14,30}, and
130 biogeochemical processes could further transform the signal prior to preservation in sedimentary
131 environments³¹.

132 To evaluate these possible alternatives, we ran 1-D early Earth photochemical models
133 where we increased CH_4 concentrations until an organic haze formed. The model utilized here
134 advances similar studies^{24,32} by analyzing hazy atmospheres after the evolution of oxygenic
135 photosynthesis. Furthermore, we consider the effect of fractal aggregate scattering by
136 hydrocarbon aerosols³³, and contrast with traditional Mie scattering results. We use these models
137 to explore how optical depth, reaction pathways, and sulfur exit channels vary as a function of
138 CH_4 concentration, and tie these atmospheric properties to candidate mechanisms for the
139 observed changes in $\Delta^{36}\text{S}/\Delta^{33}\text{S}$. Figures 3 and S8 show two sets of photochemical model
140 simulations, both varying CH_4 concentrations from 1 to 50,000 ppm, while holding CO_2
141 concentrations at 1% and ground-level O_2 concentrations at 10 ppb. The two simulations differ
142 only in their hydrocarbon particle scattering physics (see SI for a discussion of boundary

143 conditions, particle formation and scattering). For both fractal and Mie scattering cases, higher
144 CH₄ resulted in increasingly reduced atmospheres, as evidenced by decreasing OH
145 concentrations (Fig. 3A; S8A). Despite large volcanic SO₂ and H₂S fluxes, none of our model
146 atmospheres accumulated large enough concentrations of SO₂ or OCS to affect S-MIF (see SI for
147 additional discussion). The dominant contributors to opacity between 180 and 220 nm in our
148 haze-free models were CO₂ absorption and Rayleigh scattering. Prior to haze formation, most
149 photons longward of 200 nm reached the Earth surface.

150 Even when CH₄ is too low to promote haze formation (CH₄:CO₂ < 0.1), changes to CH₄
151 concentrations altered the redox chemistry and impacted S-MIF exit channels. Enhanced CH₄
152 concentrations alone do not affect S-MIF, as the CH₄ absorption spectrum does not overlap the
153 vibrational bands of SO₂ that give rise to S-MIF. Instead, increases in CH₄ provided the reducing
154 capacity to polymerize elemental sulfur, thus promoting aerosol S₈ as an exit channel.
155 Simultaneously, SO₂ replaced sulfate as the most oxidized exit channel (Fig. 3C; S8C),
156 implicating the SO₂/S₈ couple as carriers of opposite-sign S-MIF. Reaction rates for S₃
157 polymerization, excited state SO₂ formation and SO photolysis all increased with increasing CH₄
158 concentrations (Fig. 3B; S8B). If any of these reactions produces significant S-MIF, they could
159 modify the signal produced by SO₂ photolysis. Regardless of mechanism, we suggest this haze
160 free regime is the origin of the 0.9 Archean ‘reference’ slope in $\Delta^{36}\text{S}/\Delta^{33}\text{S}$.

161 At CH₄:CO₂ > 0.1, a hydrocarbon haze dramatically altered our model atmospheres. The
162 broadband absorption by this haze caused a drastic reduction in photochemical reactions, and
163 specifically a slowdown of the S cycle. In the fractal scattering case, SO₂ photolysis rates slowed
164 by nearly two orders of magnitude (Fig 3B), as photons shortward of 220 nm were scattered by
165 the stratospheric haze. By contrast, SO₂ photoexcitation to ¹SO₂ (210-327 nm) and ³SO₂ (337-

166 385 nm) remained prevalent. There are two potential sources of S-MIF variation in this regime: a
167 changing ratio of SO₂ photolysis to photoexcitation, and opacity effects arising from fewer total
168 photons. Other pathways involving multiple S atoms, such as S₃ polymerization or SO-SO dimer
169 formation, became unfeasible in the photon-starved CH₄:CO₂ > 0.1 environment.

170 For 0.1 < CH₄:CO₂ < 0.2, haze-induced shielding led to counter-intuitive decreases in the
171 CH₄ fluxes needed to support increasing CH₄ concentrations. As atmospheric CH₄ rose the haze
172 thickened, decreasing both CH₄ photolysis and the formation of radicals that destroy CH₄. The
173 haze therefore diminished the photochemical sinks for CH₄ such that larger concentrations could
174 be maintained at lower CH₄ source fluxes. This would have made atmospheres with 0.1 <
175 CH₄:CO₂ < 0.2 unstable. If a biosphere produced enough CH₄ to reach CH₄:CO₂ > 0.1, a positive
176 feedback would have ensued, increasing CH₄ concentrations until CH₄:CO₂ = ~ 0.2, at which
177 point further increases in CH₄ concentrations would have required biologically unfeasible CH₄
178 fluxes (see details in SI).

179 In both simulations, atmospheres with CH₄:CO₂ > 0.2 are unsustainable. If organic
180 particles scatter light according to Mie theory, a thick haze could be prevented by a Gaian
181 climate/CH₄ feedback²⁴ on global glaciations³⁴. If organic particles behave like fractal scatterers,
182 a thick haze would have formed a UV shield effective enough to shut down photochemical haze
183 production (see Fig. 3B and SI). In either case, we can place an upper limit of ~0.2 on the
184 atmospheric CH₄:CO₂ ratio.

185 In summary, there are two accessible, stable regimes in our photochemical simulations:
186 CH₄:CO₂ < 0.1, and CH₄:CO₂ ~ 0.2. In the first of these regimes, SO₂ photolysis was a major
187 source of S-MIF, although other potential S-MIF reactions proceeded rapidly enough to be
188 quantitatively relevant. The exit channels varied as a function of atmospheric redox state, and the

189 magnitude of S-MIF in a given exit species would be expected to vary inversely with the relative
190 mass fraction. In the second regime, the atmospheric S cycle operated slowly due to haze-
191 induced opacity that significantly decreased photolysis rates in the lower atmosphere. SO₂
192 photolysis remained a likely source of S-MIF, and the lower photon availability could have led to
193 significant SO₂ isotopologue absorption effects. S-MIF from symmetry-dependent de-excitation
194 of SO₂ also had the potential to be an important source of S-MIF in this regime. SO₂ became the
195 dominant exit channel, so its S-MIF signature should trend to 0 by mass balance considerations,
196 with correspondingly higher S-MIF magnitudes in the minor (by mass) exit channels. Transition
197 between the first and second regimes could therefore induce changes in S-MIF source
198 magnitudes, coupled with changes in the reservoirs by which S-MIF exits the atmosphere. If low
199 $\delta^{13}\text{C}_{\text{org}}$ reflects periods of enhanced methane flux, a bi-stable atmospheric transition from haze-
200 free ($\text{CH}_4:\text{CO}_2 < 0.1$) to thin haze ($\text{CH}_4:\text{CO}_2 \cong 0.2$) could explain the $\Delta^{36}\text{S}/\Delta^{33}\text{S}$ slope changes in
201 ancient sediments.

202 Consideration of these models along with the high-resolution geochemical dataset
203 presented here points to a Neoproterozoic depositional environment that includes: (1) microbial mat
204 ecosystems similar to modern mats, with intensive internal recycling of sulfur; (2) cyanobacterial
205 oxygen production and shallow water oxygenation as early as ~2.65 Ga; and (3) a link between
206 methanotrophy and S-MIF producing atmospheric chemistry, indicating a reducing atmosphere
207 with multiple episodes of organic haze formation during periods of enhanced biological CH₄
208 production. These records provide crucial evidence for the biogeochemical production and fate
209 of oxidants and reductants in the oceans and atmosphere during the critical period in Earth
210 history immediately pre-dating the first major rise in atmospheric oxygen.

211

212 **Methods**

213 Pyrite sulfur isotope compositions were determined on Ag₂S precipitates from distillation
214 with chromous chloride. Quadruple S isotope measurements were performed at the University of
215 Maryland, following the techniques described in Domagal-Goldman *et al.*²⁴, and reported as $\delta^{34}\text{S}$
216 $= ((^{34}\text{S}/^{32}\text{S})_{\text{sample}}/({}^{34}\text{S}/^{32}\text{S})_{\text{V-CDT}} - 1)$, $\Delta^{33}\text{S} = ({}^{33}\text{S}/^{32}\text{S})_{\text{sample}}/({}^{33}\text{S}/^{32}\text{S})_{\text{V-CDT}} - [({}^{34}\text{S}/^{32}\text{S})_{\text{sample}}/({}^{34}\text{S}/^{32}\text{S})_{\text{V-CDT}}]^{0.515}$,
217 $\Delta^{36}\text{S} = ({}^{36}\text{S}/^{32}\text{S})_{\text{sample}}/({}^{36}\text{S}/^{32}\text{S})_{\text{V-CDT}} - [({}^{34}\text{S}/^{32}\text{S})_{\text{sample}}/({}^{34}\text{S}/^{32}\text{S})_{\text{V-CDT}}]^{1.9}$, with values given in
218 permil (‰). Analytical uncertainties on S isotope measurements, estimated from long-term
219 reproducibility of Ag₂S fluorinations, are 0.14, 0.008, and 0.20 (1 σ) for $\delta^{34}\text{S}$, $\Delta^{33}\text{S}$, and $\Delta^{36}\text{S}$,
220 respectively. Iron speciation was determined at Newcastle University via the sequential
221 extraction techniques of Poulton *et al.*^{12,13}. Replicate extractions give an RSD of <5% for all
222 extraction steps. Total organic carbon (TOC) was measured on a Leco analyzer after treatment
223 with dilute 20% HCl to remove carbonate phases. Organic C isotopes were measured on acid-
224 treated samples by EA-IRMS, reported as $\delta^{13}\text{C} = ((^{13}\text{C}/^{12}\text{C})_{\text{sample}}/({}^{13}\text{C}/^{12}\text{C})_{\text{VPDB}} - 1)$ (‰). Replicate
225 analyses (n = 6) of an internal standard ($\delta^{13}\text{C}_{\text{org}} = -26.43\text{‰}$) gave an average value of $-26.43 \pm$
226 0.06‰ (1 σ) during the sample run.

227 The 1-D photochemical model derives from Zhanle *et al.*³⁰, but contains the organic
228 carbon species and chemistry from Domagal-Goldman *et al.*²⁴, as well as their δ two-stream
229 radiative transfer scheme. The model simultaneously solves photochemical production and loss
230 for 74 species undergoing 392 reactions, including transport by eddy and molecular diffusion
231 over a 100 km grid with 0.5 km grid spacing. We adopt the temperature, eddy diffusion, and
232 water vapor profiles from Domagal-Goldman *et al.*²⁴, leaving all other parameterizations
233 (rainout, lightning, diffusion-limited hydrogen escape, etc.) unchanged. The modern solar flux is

234 used, although sensitivity tests were run approximating the spectral character of the sun at 2.5
235 Ga. Further details, including boundary conditions, are given in the Supplementary Information.

236

237 Correspondence and requests for materials should be addressed to Aubrey L. Zerkle,
238 aubrey.zerkle@ncl.ac.uk.

239

240 **Acknowledgements**

241 We thank J. Kirschvink, J. Grotzinger, A. Knoll and the Agouon Institute for organizing and funding the
242 Agouon drilling project. We also thank Mark Thiemens and one anonymous reviewer for constructive
243 comments on the manuscript. This study was funded by the NASA Exobiology Program and NASA
244 Astrobiology Institute (A.L.Z. and J.F.). M.W.C and S.D.D-G. would like to acknowledge support from
245 the NAI Virtual Planetary Laboratory and the NASA Postdoctoral Program.

246

247 **Author Contributions**

248 A.L.Z. performed sulfur isotope analyses and spearheaded the study, M.W.C. and S.D. D-G. developed
249 and ran the atmospheric models, S.W.P. collected the samples and performed Fe speciation analyses. All
250 authors contributed to data interpretation and manuscript preparation.

251

252 **Competing Financial Interests**

253 The authors declare no competing financial interests.

254

255 **References**

- 256 1. Schroder, S., Lacassie, J. P. & Beukes, N. J. Stratigraphic and geochemical framework of the
257 Agouon drill cores, Transvaal Supergroup (Neoproterozoic-Paleoproterozoic, South Africa). *South*
258 *African Journal of Geology* **109**, 23-54 (2006).

- 259 2. Wille, M. *et al.* Evidence for a gradual rise of oxygen between 2.6 and 2.5 Ga from Mo isotopes
260 and Re-PGE signatures in shales. *Geochimica et Cosmochimica Acta* **71**, 2417-2435, (2007).
- 261 3. Godfrey, L. V. & Falkowski, P. G. The cycling and redox state of nitrogen in the Archean ocean.
262 *Nature Geoscience* (2009).
- 263 4. Kendall, B. *et al.* Pervasive oxygenation along late Archean ocean margins. *Nature Geoscience* **3**,
264 647-652 (2010).
- 265 5. Holland, H. D. The oxygenation of the atmosphere and oceans. *Philosophical Transactions of the*
266 *Royal Society B-Biological Sciences* **361**, 903-915 (2006).
- 267 6. Anbar, A. D. *et al.* A whiff of oxygen before the great oxidation event? *Geochimica et*
268 *Cosmochimica Acta* **71**, A24-A24 (2007).
- 269 7. Kaufman, A. J. *et al.* Late Archean biospheric oxygenation and atmospheric evolution. *Science*
270 **317**, 1900-1903 (2007).
- 271 8. Garvin, J., Buick, R., Anbar, A. D., Arnold, G. L. & Kaufman, A. J. Isotopic evidence for an
272 aerobic nitrogen cycle in the latest Archean. *Science* **323**, 1045-1048 (2009).
- 273 9. Reinhard, C. T., Raiswell, R., Scott, C., Anbar, A. D. & Lyons, T. W. A late Archean sulfidic sea
274 stimulated by early oxidative weathering of the continents. *Science* **326**, 713-716 (2009).
- 275 10. Altermann, W. & Nelson, D. R. Sedimentation rates, basin analysis and regional correlations of
276 three Neoproterozoic and Paleoproterozoic sub-basins of the Kaapvaal Craton as inferred from
277 precise U-Pb zircon ages from volcanic-clastic sediments. *Sedimentary Geology* **120**, 225-256
278 (1998).
- 279 11. Miyano, T. & Beukes, N. J. Phase relations of the stilpnomelane, ferriannite, and riebeckite in very
280 low-grade metamorphosed iron formations. *Geological Society of South Africa Transactions* **87**,
281 111-124 (1984).
- 282 12. Poulton, S. W. & Raiswell, R. The low-temperature geochemical cycle of iron: From continental
283 fluxes to marine sediment deposition. *American Journal of Science* **302**, 774-805 (2002).

- 284 13. Poulton, S. W. & Canfield, D. E. Ferruginous conditions: A dominant feature of the ocean
285 through Earth's history. *Elements* **7**, 107-112 (2011).
- 286 14. Ono, S. *et al.* New insights into Archean sulfur cycle from mass-independent sulfur isotope
287 records from the Hamersley Basin, Australia. *Earth and Planetary Science Letters* **213**, 15-30,
288 (2003).
- 289 15. Canfield, D. E. & Des Marais, D. J. Aerobic sulfate reduction in microbial mats. *Science* **251**,
290 1471-1473 (1991).
- 291 16. Farquhar, J., Bao, H. M. & Thiemens, M. Atmospheric influence of Earth's earliest sulfur cycle.
292 *Science* **289**, 756-758 (2000).
- 293 17. Pavlov, A. A. & Kasting, J. F. Mass-independent fractionation of sulfur isotopes in Archean
294 sediments: Strong evidence for an anoxic Archean atmosphere. *Astrobiology* **2**, 27-41 (2002).
- 295 18. Ono, S., Wing, B., Johnston, D., Farquhar, J. & Rumble, D. Mass-dependent fractionation of
296 quadruple stable sulfur isotope system as a new tracer of sulfur biogeochemical cycles.
297 *Geochimica et Cosmochimica Acta* **70**, 2238-2252 (2006).
- 298 19. Hinrichs, K.-U. Microbial fixation of methane carbon at 2.7 Ga: Was an anaerobic mechanism
299 possible? *Geochemistry Geophysics Geosystems* **3**, 1-10 (2002).
- 300 20. Thomazo, C., Ader, M., Farquhar, J. & Philippot, P. Methanotrophs regulated atmospheric sulfur
301 isotope anomalies during the Mesoarchean (Tumbiana Formation, Western Australia). *Earth and*
302 *Planetary Science Letters* **279**, 65-75 (2009).
- 303 21. Hayes, J. M. in *Early Life on Earth* Vol. 84 (ed S. Bengtson) 200-236 (Columbia University
304 Press, 1994).
- 305 22. Danielache, S. O., Eskebjerg, C., Johnson, M. S., Ueno, Y. & Yoshida, N. High-precision
306 spectroscopy of ^{32}S , ^{33}S , and ^{34}S sulfur dioxide: Ultraviolet absorption cross sections and isotope
307 effects. *Journal of Geophysical Research - Atmospheres* **113**, D17314 (2008).

- 308 23. Ueno, Y. *et al.* Geological sulfur isotopes indicated elevated OCS in the Archean atmosphere,
309 solving faint young sun paradox. *Proceedings of the National Academy of Sciences of the United*
310 *States of America* **106**, 14784-14789 (2009).
- 311 24. Domagal-Goldman, S. D., Kasting, J. F., Johnston, D. T. & Farquhar, J. Organic haze, glaciations
312 and multiple sulfur isotopes in the Mid-Archean Era. *Earth and Planetary Science Letters* **269**,
313 29-40, (2008).
- 314 25. Farquhar, J., Savarino, J., Airieau, S. & Thiemens, M. H. Observation of wavelength-sensitive
315 mass-independent sulfur isotope effects during SO₂ photolysis: Implications for the early
316 atmosphere. *Journal of Geophysical Research-Planets* **106**, 32829-32839 (2001).
- 317 26. Farquhar, J. *et al.* Isotopic evidence for Mesoarchaeon anoxia and changing atmospheric sulphur
318 chemistry. *Nature* **449**, 706-709 (2007).
- 319 27. Masterson, A. L., Farquhar, J. & Wing, B. A. Sulfur mass-independent fractionation patterns in
320 the broadband UV photolysis of sulfur dioxide: Pressure and third body effects. *Earth and*
321 *Planetary Science Letters* **306**, 253-260 (2011).
- 322 28. Zmolek, P. *et al.* Large mass independent sulfur isotope fractionations during
323 photopolymerization of (CS₂)-C-12 and (CS₂)-C-13. *Journal of Physical Chemistry A* **103**, 2477-
324 2480 (1999).
- 325 29. Domagal-Goldman, S. D. *et al.* Using Biogenic Sulfur Gases as Remotely Detectable
326 Biosignatures on Anoxic Planets. *Astrobiology* **11**, 419-441 (2011).
- 327 30. Zahnle, K., Claire, M. & Catling, D. The loss of mass-independent fractionation in sulfur due to a
328 Palaeoproterozoic collapse of atmospheric methane. *Geobiology* **4**, 271-283, doi:10.1111/j.1472-
329 4669.2006.00085.x (2006).
- 330 31. Halevy, I., Johnston, D. T. & Schrag, D. P. Explaining the structure of the Archean Mass-
331 Independent Sulfur isotope record. *Science* **329**, 204-207 (2010).

- 332 32. Pavlov A. A., Kasting J. F. and Brown L. L. UV-shielding of NH₃ and O₂ by organic
 333 hazes in the Archean atmosphere. *Journal of Geophysical Research* **106**, 1-23. (2001)
- 334 33. Wolf, E. T. & Toon, O. B. Fractal organic hazes provided an ultraviolet shield for early Earth.
 335 *Science* **328**, 1266-1268 (2010).
- 336 34. Haqq-Misra, J. D., Domagal-Goldman, S. D., Kasting, P. J. & Kasting, J. F. A revised, hazy
 337 methane greenhouse for the Archean Earth. *Astrobiology* **8**, 1127-1137 (2008).
- 338 35. Ono, S. H., Kaufman, A. J., Farquhar, J., Sumner, D. Y. & Beukes, N. J. Lithofacies control on
 339 multiple-sulfur isotope records and Neoproterozoic sulfur cycles. *Precambrian Research* **169**, 58-67
 340 (2009).
- 341 36. Fischer, W. W. *et al.* Isotopic constraints on the Late Archean carbon cycle from the Transvaal
 342 Supergroup along the western margin of the Kaapvaal Craton, South Africa. *Precambrian
 343 Research* **169**, 15-27 (2009).

344

345 **Figure Legends**

346 Figure 1. Lithologic and geochemical data for the bottom part of core GKF01, through ~2.65 to
 347 2.5 Ga sediments of the Ghaap Group (lithologies from Schröder *et al.*¹). Data include pyrite
 348 sulfur isotope values ($\delta^{34}\text{S}$, $\Delta^{33}\text{S}$, $\Delta^{36}\text{S}$, and $\Delta^{36}\text{S}/\Delta^{33}\text{S}_{\text{dev}}$, calculated as the absolute value of the
 349 deviation from a $\Delta^{36}\text{S}/\Delta^{33}\text{S}$ slope defined by the Boomplaas and Lokammona Formations),
 350 carbon isotopes of organic carbon ($\delta^{13}\text{C}_{\text{org}}$), and Fe speciation data (Tables S2 and S3). Symbols
 351 are defined in Figure 2. Grey circles are from Ono *et al.*³⁵, grey squares are from Kendall *et al.*⁴,
 352 and grey diamonds are from Fischer *et al.*³⁶.

353 Figure 2. Cross-plots for quadruple sulfur isotopes from the GKF01 section. A. $\delta^{34}\text{S}$ versus $\Delta^{33}\text{S}$
 354 values. The dotted line is the Archean reference line ($\Delta^{33}\text{S} = 0.89 \times \delta^{34}\text{S}$)¹⁴. B. $\Delta^{33}\text{S}$ versus $\Delta^{36}\text{S}$

355 values. The solid line represents a reference array with $\Delta^{36}\text{S}/\Delta^{33}\text{S}$ slope of -0.9, and the dotted
356 line represents an array with a slope of -1.5.

357 Figure 3. Photochemical model results for fractal particles. Models were run with CO_2 fixed at
358 1% and ground-level CH_4 mixing ratios from 1×10^{-6} to 0.05, displayed as $\text{CH}_4:\text{CO}_2$ ratios.

359 Shaded regions indicate unconverged solutions. A. Mixing ratios (solid lines, left axis) and
360 fluxes (dashed lines, right axis). B. Photochemical reaction rates relative to the rate at $\text{CH}_4:\text{CO}_2 =$
361 10^{-4} (non-red lines, left axis). Effective optical depth at 200 nm (solid) and 550 nm (dashed) (red
362 lines, right axis). C. Sulfur exit channels shown as fraction of total sulfur leaving the atmosphere.
363 The dotted line is the sum of exit channels shown.

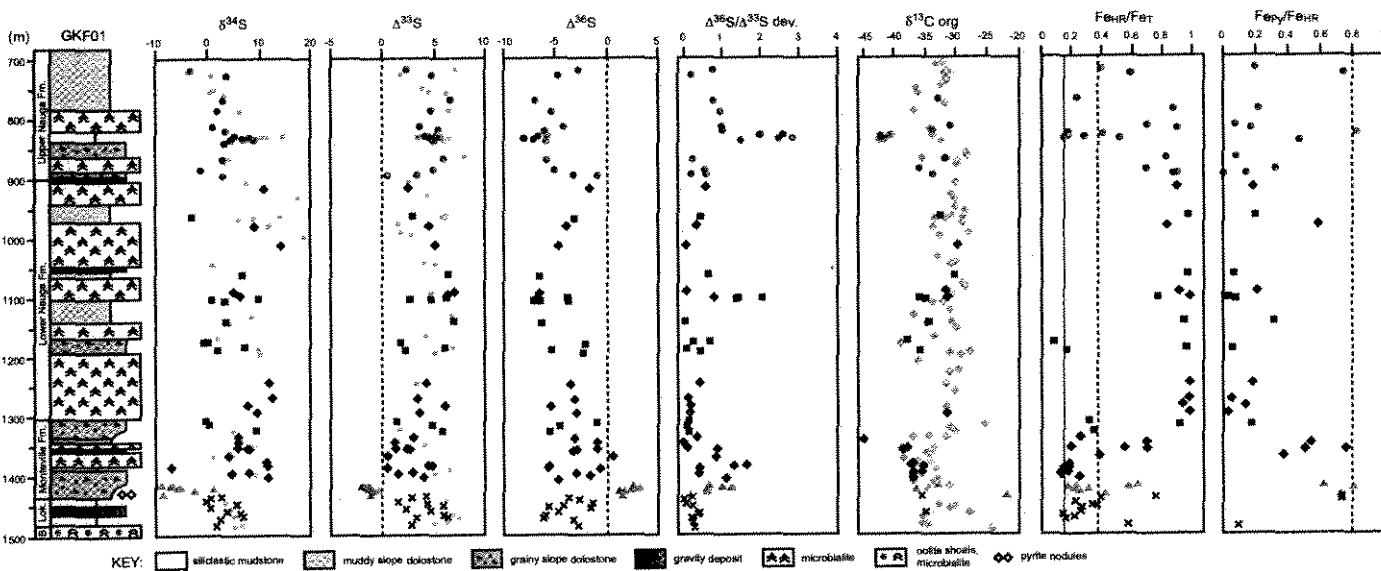


Figure 1. Zerkle et al.

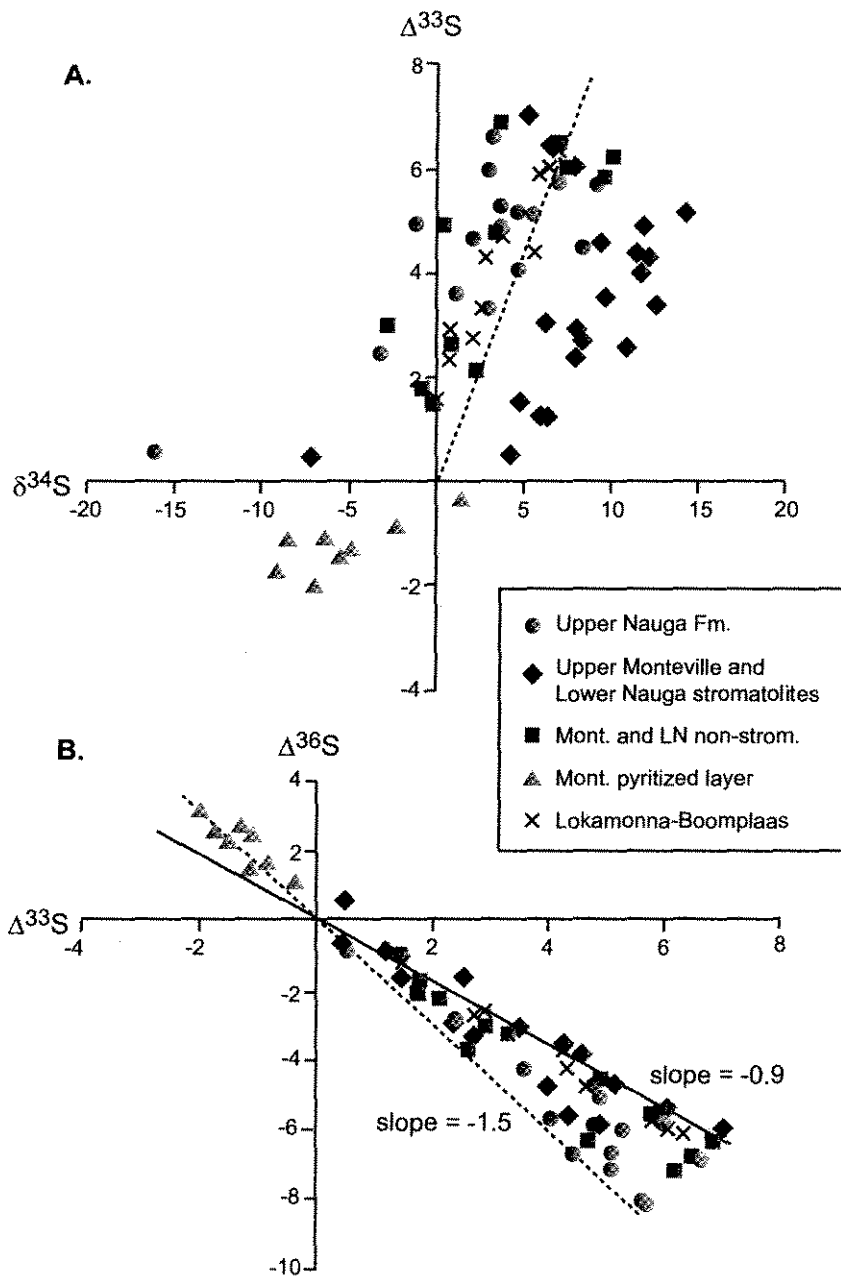


Figure 2. Zerkle et al.

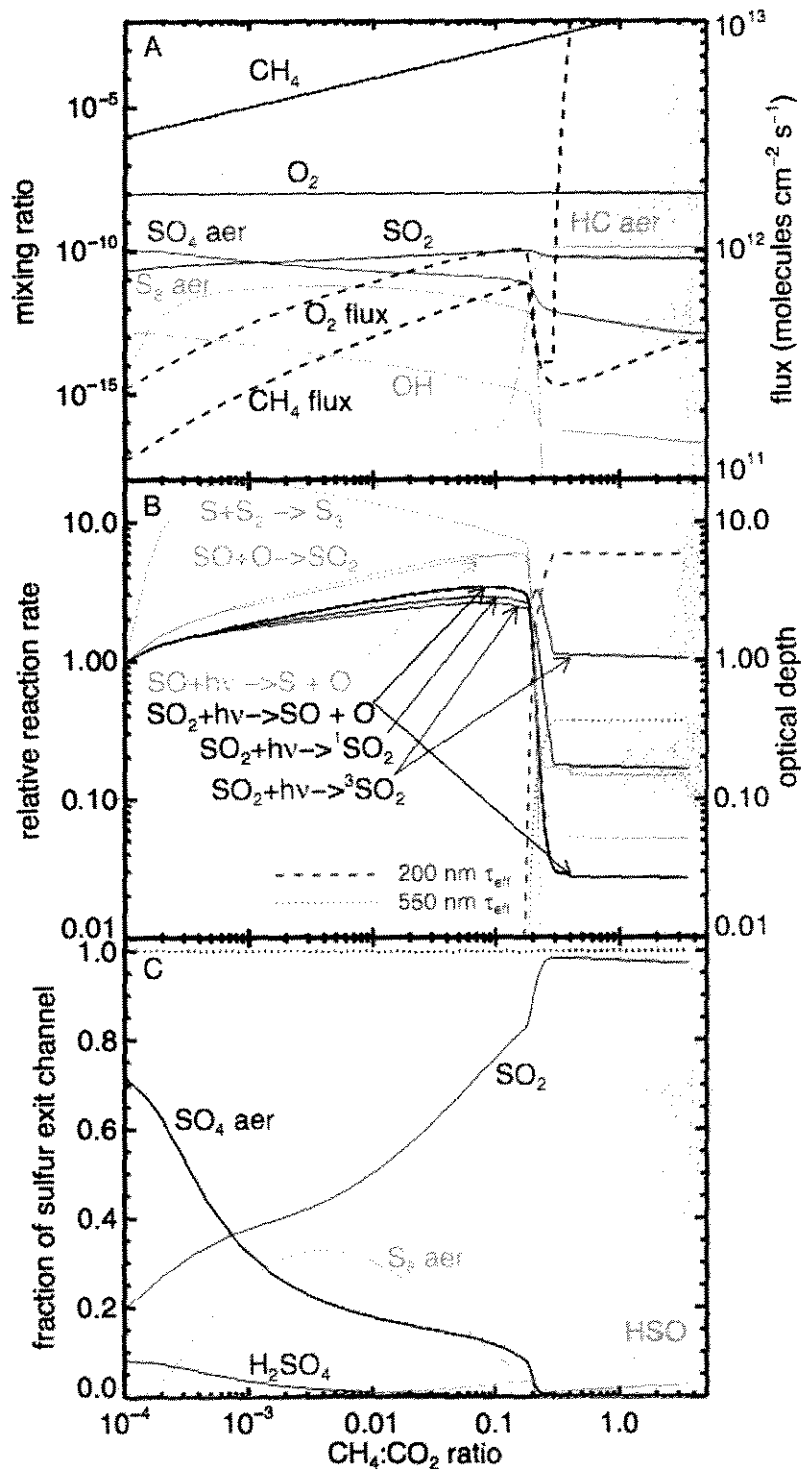


Figure 3. Zerkle et al.

